

Materials Advances

Accepted Manuscript

This article can be cited before page numbers have been issued, to do this please use: C. Fabregat, D. Velasco Castrillo, R. Bujaldón Carbó, S. Oliva, M. Ghasemi, J. Garcia Amoros, D. Volyniuk, J. V. Grazulevicius and J. Puigdollers, *Mater. Adv.*, 2025, DOI: 10.1039/D5MA01124H.



This is an Accepted Manuscript, which has been through the Royal Society of Chemistry peer review process and has been accepted for publication.

Accepted Manuscripts are published online shortly after acceptance, before technical editing, formatting and proof reading. Using this free service, authors can make their results available to the community, in citable form, before we publish the edited article. We will replace this Accepted Manuscript with the edited and formatted Advance Article as soon as it is available.

You can find more information about Accepted Manuscripts in the [Information for Authors](#).

Please note that technical editing may introduce minor changes to the text and/or graphics, which may alter content. The journal's standard [Terms & Conditions](#) and the [Ethical guidelines](#) still apply. In no event shall the Royal Society of Chemistry be held responsible for any errors or omissions in this Accepted Manuscript or any consequences arising from the use of any information it contains.

ARTICLE

Shortcut to highly π -extended optoelectronic systems based on the dibenzothiophene coreClara Fabregat,^{a,b} Roger Bujaldón,^{*a,b} Sílvia Oliva,^a Jaume Garcia-Amorós,^{a,b} Dmytro Volyniuk,^c Melika Ghasemi,^c Juozas V. Grazulevicius,^c Joaquim Puigdollers,^d Dolores Velasco ^{*a,b}Received 00th January 20xx,
Accepted 00th January 20xx

DOI: 10.1039/x0xx00000x

The Scholl reaction stands as a versatile tool to synthesize multiple π -extended systems via intramolecular C-C oxidative couplings. A prime example is the expansion of dibenzothiophene to polycyclic butterfly-shaped heterocycles, which claim key characteristics in diverse optoelectronic applications. Herein we describe a protocol from commercial tetrabromothiophene based on sequential one-pot Suzuki-Miyaura reactions followed by the Scholl reaction. This strategy permits rapid access to complex constructions fusing up to 11 rings in just two steps and improved yields. The proposed π -extensions successfully reduced the HOMO energy levels in the solid state to align with the gold work function (5.1 eV), while offering tunable photophysical properties. Remarkably, phenanthrene as scaffold endowed the core with a hole mobility value of $7 \times 10^{-5} \text{ cm}^2 \text{ V}^{-1} \text{ s}^{-1}$ in OTFTs and excellent air-stability, with a shelf lifetime exceeding one year. Moreover, the inclusion of sulfurated units unlocked room temperature phosphorescence under oxygen-free conditions, a highly sought-after characteristic in metal- and halogen-free constructions. Their RTP quantum yields when introduced into a Zeonex matrix are as high as 14%, with oxygen-sensitive photoluminescence that goes from deep-blue to yellow-orange. Altogether, this strategy holds great potential and versatility in developing adaptable materials for multiple functionalities.

Introduction

Organic materials provide unique characteristics that set them apart from their inorganic competitors, making them pivotal in next-generation electronics. Their inherent assets encompass from low-cost production processes to the fabrication of large-area and flexible devices.^{1–3} Moreover, their optoelectronic features can be easily adapted from a structural point of view to match the envisioned application.

For organic semiconductors, π -conjugated systems with adequate energy levels generally grant a steady π - π stacking, translating into an efficient and fast charge transport.^{4,5} Thiophene is a recognized building block in the field of organic electronics^{6–9}. Indeed, nuclei such as benzothieno[3,2-*b*][1]benzothiophene (BTBT)^{10–14} or dinaphtho[2,3-*b*:2',3'-*f*]thieno[3,2-*b*]thiophene (DNNT)^{15–18} are clear examples of thiophene-containing heterocycles currently acknowledged as top-performing organic semiconductors. Alternative π -expanded systems comprising branched and twisted architectures based on diphenanthro[9,10-*b*:9',10'-*d*]thiophene (DPT) are equally engaging. Synthetically, the production of this

latter core involves a 4-fold coupling of aromatic moieties to tetrabromothiophene (TBT), generally through the Suzuki-Miyaura reaction, and a subsequent intramolecular cyclization via the Scholl reaction¹⁹ (Scheme 1). Considering the easy availability of TBT as starting material and the immense library of aromatic commercially-available boronic acids, this strategy opens the way to diverse and tailored materials. So far, this approach has been exploited with assorted polycyclic structures.^{20–32}

The DPT nucleus **3** features a butterfly-shaped π -system that deviates from planarity due to the steric hindrance between the C–H bonds in positions 1 and 17 (Ar₂ in Scheme 1), a characteristic that is generally avoided in organic electronics. Regardless, the successful integration of some derivatives as hole transporting materials in devices encompassing single crystal FETs²² and perovskite solar cells³³ certainly proves their potential. Non-planar π -conjugated systems, apart from offering alternative packing arrangements,³⁴ can also circumvent the insolubility issues that hamper some top-performing materials for their use in more economical solution-processed devices.^{35–37} Moreover, this core has been recently confirmed as a metal- and halogen-free platform towards room temperature phosphorescence (RTP),³⁸ a highly sought-after feature in applications like phosphorescent OLEDs, data encryption and oxygen sensing.^{39–42} Given the multifunctionality of this core, the access to diverse and more complex structures was appealing, especially via a versatile and straightforward synthetic route encompassing a broader scope of substituents.

^a Grup de Materials Orgànics, Departament de Química Inorgànica i Orgànica, Secció de Química Orgànica, Universitat de Barcelona, Martí i Franquès 1, E-08028, Barcelona, Spain.

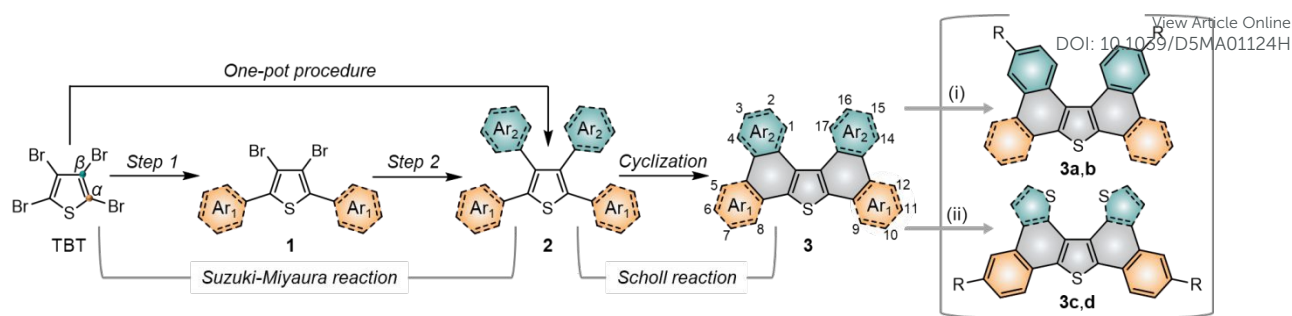
^b Institut de Nanociència i Nanotecnologia (IN²UB), E-08028, Barcelona, Spain.

^c Department of Polymer Chemistry and Technology, Kaunas University of Technology, Barsausko 59, Kaunas, Lithuania.

^d Dept. Enginyeria Electrònica, Universitat Politècnica de Catalunya, Jordi Girona 1–3, E-08034, Barcelona, Spain.

Supplementary Information available: [details of any supplementary information available should be included here]. See DOI: 10.1039/x0xx00000x





Scheme 1. Envisioned synthetic route towards diverse π -extended derivatives based on the dibenzothiophene nucleus (in grey) from the commercially available tetrabromothiophene (TBT). The structures in the right depict the DPT derivatives (**3a–d**) targeted in this work, based on: (i) the expansion of aromatics in positions α (Ar_1 in orange) or (ii) the inclusion of thiophene-derived aromatics in β (Ar_2 in green).

With this in mind, we designed two sets of compounds: (i) derivatives **3a,b**, based on the expansion of the π -system through the aromatics in positions α of thiophene, especially those fusing numerous rings; (ii) derivatives **3c,d**, based on the incorporation of sulfurated heterocycles in β to target more planar structures. Indeed, the substitution of C–H of phenyls by sulfur lessens the steric hindrance in that position, as demonstrated by some reported crystal structures.⁴⁴ Nevertheless, either the incorporation of bulky aromatic extensions or the construction of more planar π -extended heterocycles could easily derive into major solubility problems. Thus, we introduced long alkyl chains to ensure reasonable solubility of the final products. Moreover, alkyl chains greatly modulate intermolecular interactions, which are key in solid-state properties.^{45–50} Overall, these designs imply a heterogeneous substitution to α and β positions of thiophene, requiring two consecutive two-fold cross-couplings instead of a homogeneous tetrasubstitution. In this step, we evaluated the viability of a one-pot procedure towards a more direct synthetic route.⁵¹ Fusing the central thiophene ring with additional thiophene derivatives at the periphery, however, represented a tricky point. Indeed, the precedents on thiophene-derived scaffolds coupled to tetrabromothiophene via the Suzuki-Miyaura reaction are scarce and often infructuous, especially to positions β .⁵² Alternatively, the few successful examples substitute the corresponding boronic acids for their respective pinacol esters⁵³ or trihydroxyboronate salts⁴⁴. The Stille⁵⁴ and Kumada^{55–56} cross-coupling reactions are also valid to achieve so. Since boronic acids are generally more accessible, though, we surveyed different synthetic conditions to prioritize their use.

The potential of this strategy is confirmed with the synthesis of the target π -extended compounds via sequential one-pot Suzuki-Miyaura and Scholl reactions, and the assessment of their photophysical, electrochemical and thermal properties. All derivatives were also investigated in two high-impact areas: as semiconductor materials in organic thin-film transistors (OTFTs) and as pure halogen-free organic emitters displaying RTP.

Experimental section

The information regarding chemicals, synthetic procedures and characterization is detailed in the Supplementary Information.

Structural characterization

¹H NMR spectra were collected using either a Varian Mercury or a Bruker Avance III spectrometer operating at 400 MHz. ¹³C NMR measurements were carried out on a Bruker Avance III system at 100 MHz. All spectra were analysed with MestReNova software (version 14.0.0-23239), using the solvent signal as reference. Mass spectrometry was conducted on an Applied Biosystems MDS SCIEX 4800 instrument in reflector mode via MALDI-TOF. Single-crystal X-ray diffraction data were collected using a Bruker D8 Venture system equipped with a multilayer monochromator and a Mo K α microfocus source ($\lambda = 0.71073$ Å). Data integration was performed using the Bruker SAINT software package with a narrow-frame algorithm. Structure solution and refinement were carried out using the SHELXTL software suite.

Electrochemical and thermal characterization

Cyclic voltammetry measurements were conducted for the electrochemical characterization under argon atmosphere and quiescent conditions at 100 mV s^{−1} using a cylindrical three-electrode cell connected to a potentiostat/galvanostat (Autolab PGSTAT30) with NOVA software. An Ag/Ag⁺ electrode (10^{−3} M AgNO₃ in acetonitrile) was used as the reference, a glassy carbon electrode was employed as the working one, while a platinum wire served as the counter electrode. The analysed compounds were dissolved in distilled dichloromethane (1 mM) with tetrabutylammonium hexafluorophosphate (TBAP) as the supporting electrolyte (0.1 M). All voltammetries were referred to the Fc⁺/Fc redox couple. Ionization potentials (IP) were estimated from the onset of the first oxidation peak ($E_{\text{onset}}^{\text{ox}}$) as: $\text{IP} = E_{\text{onset}}^{\text{ox}} + 5.39$ eV, with 5.39 eV being the energy level of the Fc⁺/Fc couple on the Fermi scale.⁵⁷ Electron affinities (EA) were estimated as $\text{EA} = \text{IP} - E_{\text{gap}}^{\text{opt}}$, in which the optical band gap ($E_{\text{gap}}^{\text{opt}}$) was extracted from the onset wavelength of the UV–Vis absorption spectrum. Ionization potentials in films (IP_{film}) were acquired via electron photoemission spectroscopy in air. The samples were prepared by vacuum deposition (< 10^{−6} mbar) over glass slides coated with fluorine-doped SnO₂. The setup was composed of a 6517B Keithley electrometer, an ASBN-



D130-CM deep UV deuterium light source and a CM110 1/8m monochromator. The photoelectron emission spectra were acquired by irradiating the samples with increasing excitation energies, while monitoring the resulting photoemission current as a function of the excitation energy. Differential scanning calorimetry (DSC) and thermogravimetric analysis (TGA) thermograms were acquired under nitrogen atmosphere in a scan rate of 10 °C min⁻¹, using a TA Instruments Q2000 calorimeter and a TA Instruments Q50, respectively.

Charge transport characterization

Samples for time-of-flight (TOF) measurements were prepared by vacuum evaporation (< 10⁻⁶ mbar) onto glass substrates coated with a 100 nm layer of indium-tin oxide (ITO). Subsequently, an aluminum layer (70 nm) was analogously deposited through a shadow mask to define the electrodes. Charge carriers were generated using a pulsed Nd:YAG laser (EKSPLA NL300) operating at an excitation wavelength of 355 nm and a pulse duration of 3–6 ns. The surface potential was controlled with a Keithley 6517B electrometer, and photocurrent transients were recorded using a Tektronix TDS 3032C oscilloscope. The carrier transit times (t_{tr}) were determined from the inflection point observed in the transient curve plotted on a log–log scale. Charge carrier drift mobility (μ_{TOF}) was calculated using the relation $\mu_{TOF} = d^2/(U \cdot t_{tr})$, where d is the film thickness and U is the applied voltage at the moment of photoexcitation. The thickness of the films were measured using a Profil3D profilometer. Zero-field mobilities ($\mu_{0,TOF}$) and the field-activation parameter (α) were extracted using the Poole–Frenkel-type relation $\mu_{TOF} = \mu_{0,TOF} \cdot \exp(\alpha \cdot E^{1/2})$, where E is the applied electric field.

OTFT devices were fabricated in a bottom-gate, top-contact configuration on thermally oxidized crystalline SiO₂/Si wafers (SiO₂ thickness of ca. 135 nm) coated with a polystyrene (PS) layer. The pre-treatment of the substrate and deposition of PS were carried out using a reported method.⁴⁶ The organic semiconductors were deposited by thermal evaporation under vacuum (< 10⁻⁶ mbar). Sublimation temperatures were monitored for each compound to stabilize the deposition rate at 0.3 Å s⁻¹ until reaching a film thickness of 75 nm. Gold contacts were subsequently deposited in a separate vacuum chamber using a shadow mask to define the device architecture. Each substrate contained 16 analogous OTFT devices, with channel dimensions of 2 mm (W) and 80 μm (L). Electrical characterization was performed under ambient conditions in the dark with a Keithley 2636A source meter. Charge carrier mobility values were extracted in the saturation regime (μ_{sat}) as $I_D = (\mu_{sat} C_{ox} (V_G - V_{th})^2 W)/2L$, where C_{ox} is the capacitance per unit area of the gate insulator. All devices were stored under ambient conditions in the dark.

Photophysical characterization

Absorption and emission spectra in dichloromethane were collected at room temperature in a Varian Cary UV-Vis-NIR 500E spectrophotometer and a PTI 810 fluorimeter, respectively. Fluorescence quantum yields in solution ($\Phi_{f,sol}$) were quantified

in toluene with an integrating sphere using an Edinburgh Instruments FLS980 fluorescence spectrophotometer. Films for the photophysical characterization were prepared through the drop-casting method, in which the components were dissolved in toluene and carefully deposited onto quartz substrates to ensure full surface coverage. The solvent was then allowed to evaporate slowly under ambient conditions to promote uniform film formation. The composition of the drop-casted solutions was as follows: fluorophore (1 mg mL⁻¹) for the characterization in the solid state, and Zeonex (4 mg mL⁻¹) and fluorophore (1 wt% with respect to Zeonex) for Zeonex-based films. Absorption and emission spectra in films were collected using a PerkinElmer Lambda 35 UV/Vis spectrophotometer and an Edinburgh Instruments FLS980 fluorescence spectrophotometer, respectively. Fluorescence quantum yields in the solid state were also quantified with an integrating sphere.

Results and discussion

Synthesis

As stated, we designed two types of derivatives incorporating: (i) large aromatic scaffolds in α positions (9-phenanthrenyl and 4-dibenzothieryl for **3a** and **3b**, respectively) and 4-hexylphenyl moieties in β positions to preserve some solubility; (ii) 4-alkylphenyl scaffolds in α positions and sulfurated heterocycles in β positions to target more planar structures (4-phenyloxyphenyl and 2-benzothieryl for **3c** and 4-methylphen-2-yl and 5-hexylthien-2-yl for **3d**). For this, we first surveyed different established methods in the synthesis of intermediates **1a–d** to identify the most suitable conditions. Table 1 summarizes the main synthetic results and conditions towards the disubstituted intermediates **1a–d**.

The use of Pd(PPh₃)₂Cl₂ as catalyst, PPh₃ as ligand and K₂CO₃ as base in a mixture of DMF/water as solvent (cond. A), being successful for tetrasubstitutions in 9H-carbazole⁵⁸ and thiophene³⁷, was optimal for incorporating 9-phenanthrene in **1a**, but induced debromination as a side-reaction when incorporating heteroatom-containing moieties, resulting in by-products **5b,c** instead of the expected **1b,c**. As reported in the literature, β positions with respect to the heteroatom are particularly vulnerable to dehalogenation in this type of systems.^{59–63} Thus, the use of DMF/water was not suitable for a 2-fold all-encompassing coupling to TBT. The substitution of DMF by THF with Pd(PPh₃)₄ as catalyst in milder conditions (cond. B) deactivated the dehalogenation pathway, successfully yielding compounds **1b,c** and in a ca. 45%. It was also beneficial in the case of **1d**, increasing from 42 to 58%, while **1a** dropped from 56 to 26%. The use of toluene/water with Pd(PPh₃)₂Cl₂/PPh₃ (cond. C), which was similarly used in the literature,⁵¹ underperformed in all cases, majorly leading to the monosubstituted counterpart **4**. The combination of toluene with methanol and Pd(PPh₃)₄ as catalyst (cond. D)^{23,64} resulted in the choicest option, with yields surpassing the aforementioned conditions. Particularly, the yields of **1b** and **1d** raised from 46 and 58% to 70 and 83%, respectively, in relation to THF/water. Therefore, the subsequent coupling towards



ARTICLE

Materials Advances

Table 1. Comparison between the proposed Suzuki-Miyaura conditions (A–D) in the synthesis of the disubstituted intermediates **1a–d**. The yields of both intermediates and main by-products (**4,5**) refer to the isolated yields.

Condi- tion	Solv ₁ : Solv ₂	Ratio (v/v)	1 a (%)	By- pro- d. (%)	1 b (%)	By- pro- d. (%)	1 c (%)	By- pro- d. (%)	1 d (%)	By- pro- d. (%)
A ^a	DMF: H ₂ O	8:1	5 6	(-) ^c	(-) 5b ^c	71 (5b)	69 (5c)	4 2	(-) ^c	
	THF:		2	23	4		4	5		

structure **2** was performed using these conditions and the second best-performing ones for comparison, i.e. DMF/water for **2a** and THF/water for **2b–d**. Table 2 compiles the main results. The use of toluene/methanol greatly ameliorated the yields of all tetrasubstituted derivatives. This is especially notable for **2b**, increasing from 35 to 60%. The inclusion of sulfurated scaffolds in β positions was further improved with Pd(AcO)₂ as catalyst, SPhos as ligand and potassium phosphate as base (Cond. E).⁵² Remarkably, the one-pot process did not only shorten the synthetic route, but also granted higher yields of precursors **2a–d** than the 2-step procedure. The choice of toluene/methanol as solvent grants a more universal method to introduce a diverse array of scaffolds in a one-pot way.

The Scholl reaction was carried out under standard conditions, as shown in Scheme 2. These conditions were successful in yielding compounds **3a** and **3c** in an 81 and 74%, respectively, but failed for the other two due to polymerization and other side reactions. To avoid these, we reduced the temperature to 0 °C, achieving an excellent 91% for **3b** and a 14% for **3d**. The unprecedented chlorination at aliphatic positions in **3d** even at low temperature, which was confirmed via NMR spectroscopy (Fig. S1), could expand the applicability of the Scholl reaction. Overall, this synthetic strategy permits the construction of highly extended heterocycles up to 11-ring from TBT in just two steps.

It should be highlighted that, despite the bulkiness and π -extension of **3a**, its non-planarity makes it highly soluble in all type of organic solvents, including non-polar examples like hexane (ca. 3 mg mL⁻¹ at room temperature). This characteristic is prone to facilitating its implementation in solution-processed displays for a low-cost and greener manufacturing.

Single-crystal analysis

The single-crystal analysis of **3a** permitted to get further insight into its structure and arrangement. It could be crystallized in space group *P*-1 of the triclinic system in two alternative arrangements, depending on the solvent mixture: the first one

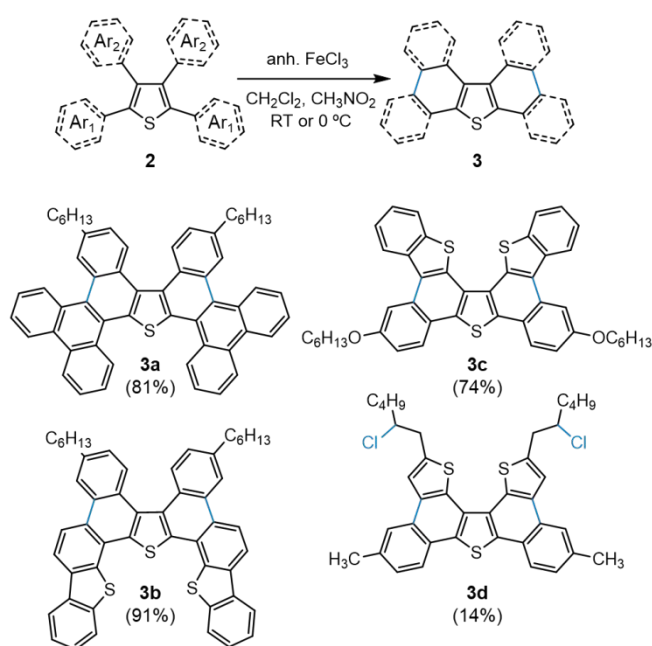
Table 2. Comparison between the proposed Suzuki-Miyaura conditions in the synthesis of the tetrasubstituted intermediates **2a–d**. All values refer to the isolated yields.

Substituent		Method ^a	Yield (%)			
R ₁	R ₂	Solv ₁ :Solv ₂	1	2 ^b	Global ^c	One-pot ^d
a		DMF:H ₂ O	56	55	31	70
		Tol.:MeOH	51	86	44	73
b		THF:H ₂ O	46	76	35	53
		Tol.:MeOH	70	86	60	69
c		THF:H ₂ O	45	52	23	34
		Tol.:MeOH	38	71 ^e	27 ^e	46 ^e
d		THF:H ₂ O	58	(-) ^f	(-) ^f	(-) ^f
		Tol.:MeOH	83	78 ^e	65 ^e	76 ^e

^a Conditions: (A) DMF:H₂O 8:1 v/v with Pd(PPh₃)₂Cl₂ (5 mol%) and PPh₃ (10 mol%) at 110 °C; (B) THF:H₂O 6:1 v/v with Pd(PPh₃)₄ (5 mol%) under reflux; (D) Toluene:MeOH 3:1 v/v with Pd(PPh₃)₄ (5 mol%) under reflux. ^b Single-step yield of **2** from intermediate **1**. ^c Yield of **2** comprising steps 1 and 2. ^d Yield of **2** on the one-pot process from TBT. ^e Cond. E: the second coupling implied the addition of benzothien-2-ylboronic acid in **1c** or 5-hexylthienyl as a pinacol ester⁶⁵ in **1d** (4 eq.), Pd(AcO)₂ (5 mol%) as catalyst, SPhos (20 mol%) as ligand and K₃PO₄ (4 eq.) as base. ^f These conditions were not suitable for the coupling of pinacol boronic esters.

was obtained from a mixture of hexane and dichloromethane (Fig. 1a), and the second one, from dichloromethane and ethanol (Fig. 1b). Both structures embedded solvent molecules.





Scheme 2. Cyclization to compounds **3a–d** via the Scholl reaction.

As observed, they corroborate the non-planarity of **3a**, with torsion angles around 25° . The π - π stacking in this type of materials generally takes place between dimers comprising both atropoisomers, since this combination offers a better match. The first packing present π -stacking distances between atropoisomers that go from 3.3 to 3.9 Å, whereas the closest π - π interaction between dimers comes from slipped stacking distances of 3.87 Å, with additional stabilization from alkyl C-H \cdots π and edge-to-edge interactions. The second crystal

emphasizes even more the potential of **3a**, with consistent π - π stacking interaction between atropoisomers as close as 3.3 Å. The dimers establish edge-to-face interactions between each other with distances up to 3.66 Å, with a resulting packing that could be assimilated to a γ type.^{66,67} This type of packing presents two different π - π stacking directions, which endows the crystal with alternative hopping routes in charge-transporting applications. The crystallographic data is detailed in the Supplementary information.

Electrochemical and thermal properties

Table 3 compiles the electrochemical and thermal properties of **3a–c** and those of DPT for comparison. Their optical band gaps, extracted from the onset of their absorption spectra in dichloromethane solutions, are quite divergent. Derivative **3a** presents the smallest one of 2.74 eV, suggesting a higher conjugation and extension of the π -system despite its non-planarity. The values for those including sulfurated extensions (**3b–d**) go from 3.03 to 3.32 eV, which are still lower than the 3.33 eV observed for DPT. As shown in the cyclic voltammograms (Fig. S3), all compounds underwent an oxidation process that was used to estimate their IP values, being around 5.9 eV. The IP values were also determined in the solid state via photoelectron emission spectrometry (Fig. S4), exhibiting a considerable decrease with respect to the values obtained for solutions presumably due to an effective π -stacking and delocalization. In fact, they cover the range from 4.80 to 5.21 eV, thus lowering the value relative to that of the DPT nucleus (5.96 eV). Thus, the proposed π -extensions place this core closer to the gold work function (ca. 5.1 eV). A neutral p-type semiconductor should feature an IP higher than 4.9 eV.⁴ Otherwise, a shallow HOMO energy level would make it prone

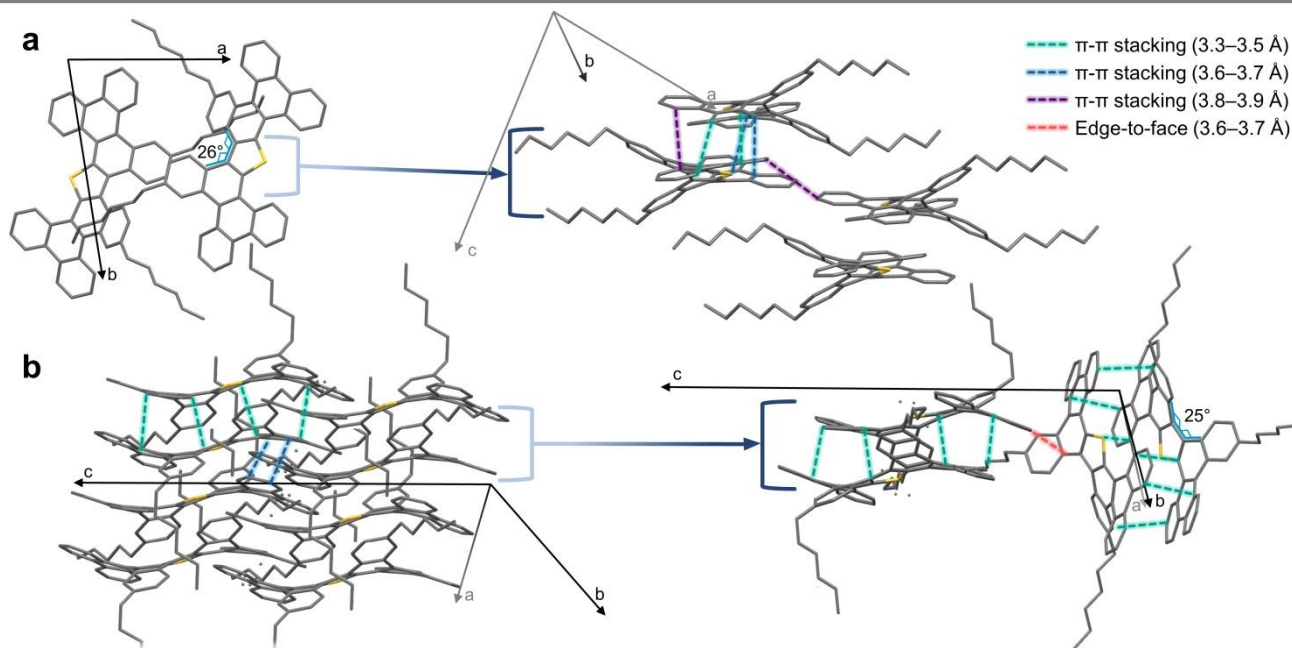


Fig. 1. Single-crystal structures of compound **3a** crystallized from: (a) hexane and dichloromethane and (b) dichloromethane and methanol. Both structures are displayed from two points of view, with the corresponding cell axes, representative π - π stacking interactions and torsion angles. Hydrogen atoms and solvent molecules are omitted for clarity.



ARTICLE

Materials Advances

Table 3. Electrochemical and thermal characteristics of compounds **3a–d**. Data corresponding to the DPT nucleus is also added for comparison.

	$E_{\text{gap}}^{\text{opt}}$ (eV) ^a	$E_{\text{onset}}^{\text{ox}}$ (V) ^b	IP (eV) ^c	EA (eV) ^d	IP _{film} (eV) ^e	T_m (°C) ^f	T_d (°C) ^g
DPT ³⁷	3.33	0.83	6.22	2.89	5.96	265	257
3a	2.74	0.50	5.89	3.15	5.01	-	425
3b	3.03	0.50	5.89	2.86	4.87	271	468
3c	3.32	0.54	5.93	2.61	4.80	246	415
3d	3.27	0.57	5.96	2.76	5.21	254	260

^a Optical energy gaps, estimated from the absorption spectrum (Fig. S10c). ^b Onset oxidation potentials vs. Fc⁺/Fc, determined via CV in 1 mM solutions in CH₂Cl₂. ^c Ionization potentials in CH₂Cl₂, estimated as IP = $E_{\text{onset}}^{\text{ox}}$ vs. Fc⁺/Fc + 5.39. ^d Electron affinities in CH₂Cl₂, estimated as EA = IP – $E_{\text{gap}}^{\text{opt}}$. ^e Ionization potentials in the solid state, extracted from the photoelectron emission spectra of vacuum-deposited films. ^f Melting temperatures obtained from DSC at a scan rate of 10 °C min⁻¹. ^g Decomposition temperatures obtained from the 5% weight loss in TGA at a heating rate of 10 °C min⁻¹.

to reducing ambient oxygen in the presence of humidity. Consequently, compounds **3a** and **3d** are the fittest to the gold work function while granting long-term electrochemical stability. Apart, all derivatives excel in terms of thermal stability, with **3a–c** exhibiting T_d values beyond 400 °C based on a 5% weight loss in thermogravimetric analysis (TGA). Considering that the value for DPT is 257 °C, the proposed π -extensions effectively increase the thermal stability of the main nucleus, and therefore are appropriate for a vacuum-deposition process. Their melting points (T_m), determined via differential scanning calorimetry (DSC), were significantly higher than room temperature, i.e. 271, 246 and 254 °C for **3b–d**, respectively. In the case of **3a**, if any, it was not detected below 300 °C. The DSC and TGA curves are represented in Figures S5 and S6, respectively. The characteristics of compounds **3a–d** anticipated great potential in the optoelectronic field. Thus, we evaluated the performance of these compounds as organic materials for two different functionalities: for semiconductor layers in OTFT devices and as RTP emitters for sensing or lighting displays.

Semiconductor properties

The semiconductor properties of compounds **3a–d** were dually surveyed using the time-of-flight (TOF) technique and integrated in OTFT devices. Table 4 collects the charge mobility values extracted from both techniques as well as the OTFT characteristics. The transient curves acquired via TOF in the

linear scale presented dispersive patterns, so the transient times were picked from the photocurrent transients in the log-log scale (Figs. S7 and S8). All the materials behaved as p-type semiconductors, with **3a** showing the best $\mu_{h,\text{TOF}}$ with an inherent value of $8.3 \times 10^{-5} \text{ cm}^2 \text{ V}^{-1} \text{ s}^{-1}$ at an applied electric field of $6 \times 10^5 \text{ V cm}^{-1}$. Compound **3d** exhibited slightly lower values, while **3b,c** underperformed with a $\mu_{h,\text{TOF}}$ in the order of $5 \times 10^{-6} \text{ cm}^2 \text{ V}^{-1} \text{ s}^{-1}$. These preliminary results suggest the potential of this type of constructions as semiconductors regardless of the planarity of the π -system.

In OTFTs, the organic materials were deposited under vacuum over polystyrene (PS)-coated SiO₂/Si substrates in a standard bottom gate-top contact geometry. The incorporation of a PS layer at the dielectric/semiconductor interface is a well-known strategy to reduce the wettability of the dielectric and promote improved molecular order and morphology.^{68,69} The mobility values extracted for **3a,b** were consistent with those estimated from TOF measurements. Specifically, compound **3a** showed an analogous $\mu_{h,\text{avg}}$ of $6.3 \times 10^{-5} \text{ cm}^2 \text{ V}^{-1} \text{ s}^{-1}$, whereas **3b** underperformed with a $\mu_{h,\text{avg}}$ of $4.6 \times 10^{-6} \text{ cm}^2 \text{ V}^{-1} \text{ s}^{-1}$. Fig. 2a,b displays the OTFT characteristics of **3a** both at the initial measurement and after one year of storage. As observed, **3a** maintains nearly ideal behavior with highly linear characteristics. It also demonstrates remarkable air stability, retaining comparable parameters after one year of shelf storage under ambient conditions. The evolution of its $\mu_{h,\text{avg}}$ over time is represented in Fig. S9a. Indeed, **3a** possesses the most appropriate IP in the solid state, being the closest to the gold work function while remaining low-lying enough to ensure air stability. Besides, its single-crystal structures reveal favorable π -stacking regardless of its non-planarity. On the other hand, compound **3c** increased the inherent TOF mobility by an order of magnitude when incorporated in an OTFT prototype, whereas **3d** could not be measured due to the poor quality of the deposited layers. The OTFT characteristics of compounds **3b,c** are shown in Fig. S9b,c. Although the extracted hole mobility values remain lower than those of top-performing materials, these are still noteworthy due to their unique, non-planar structural features. Furthermore, this approach offers promising opportunities for the development of stable and easily processable materials, thanks to its straightforward engineering potential.

Photophysical properties

An equally sought-after feature of DPT-based structures resides on their photoluminescence, especially RTP.³⁷ For this, we

Table 4. Hole transporting characteristics of compounds **3a–d** extracted from the TOF technique and PS-coated OTFT devices.

	$\mu_{h,\text{TOF}}$ (cm ² V ⁻¹ s ⁻¹) ^a	$\mu_{h,\text{OTFT}}$ (cm ² V ⁻¹ s ⁻¹) ^b	α (cm ⁻¹ V ^{-1/2} s ^{1/2}) ^c	$\mu_{h,\text{max}}$ (cm ² V ⁻¹ s ⁻¹) ^d	$\mu_{h,\text{avg}}$ (cm ² V ⁻¹ s ⁻¹) ^e	V_{th} (V) ^e	$I_{\text{on}}/I_{\text{off}}$ (A/A) ^d
3a	8.3×10^{-5}	5.5×10^{-6}	0.0045	6.9×10^{-5}	$(6.3 \pm 0.3) \times 10^{-5}$	11 ± 2	10 ³
3b	5.0×10^{-6}	1.8×10^{-6}	0.0009	5.1×10^{-6}	$(4.6 \pm 0.3) \times 10^{-6}$	–9	–



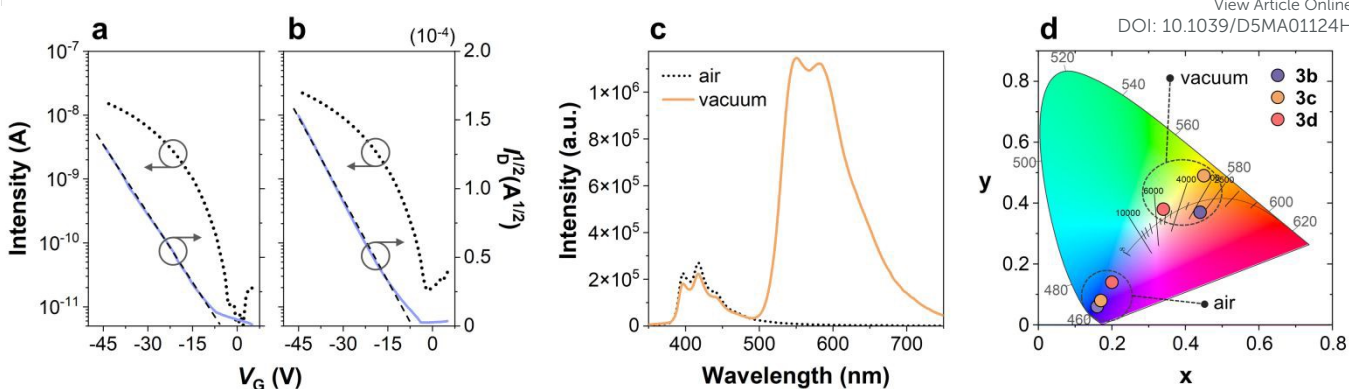


Fig. 2. Transfer ($V_D = -40$ V) and saturation characteristics of a representative PS-coated OTFT based on derivative **3a**, measured on: (a) day 36 and (b) day 365 after fabrication. (c) Photoluminescence of **3c** (1% wt.) dispersed into a Zeonex film under air and vacuum. (d) CIE coordinates of compounds **3b–d** in Zeonex under air and vacuum.

surveyed the luminescent properties of compounds **3a–d** in different media, as compiled in Table 5. Analogously, the characteristics of precursors **2a–d** were also surveyed for comparison (Table S3). All compounds emit within the UV-blue region when dissolved in toluene except for **3a**, whose emission red-shifts to the blue-green due to the effective π -conjugation with the phenanthrene scaffolds. Compound **3a** also exhibits the highest fluorescence quantum yield ($\Phi_{f,DCM} = 14\%$), surpassing that of DPT. In the solid state, the emission of all compounds undergo a bathochromic shift into the green region, accompanied by the decrease in $\Phi_{f,filim}$ due to the intermolecular interaction. The exception is the $\Phi_{f,filim}$ of **3b**, which slightly increases from 4.2 to 5.9%. On the other hand, Φ_f of the non-cyclized analogs **2a–d** are below 2% regardless of the medium. All absorption and emission spectra are compiled in the Supplementary Information.

For RTP analysis, we evaluated the molecular dispersions of all compounds in a polymeric matrix of Zeonex with a concentration of 1% wt. under air and vacuum conditions. Zeonex performs as a rigid and inert host that quenches vibrational relaxation processes, promoting an emissive decay from the triplet to the ground state in the absence of oxygen.

Emission of compound **3a** was equivalent under both conditions, thus discarding the presence of RTP for this particular structure (Fig. S12a). Contrarily, compound **3c** displayed the largest I_{vac}/I_{air} ratio, which quantifies the difference of emission intensity between vacuum and air equilibrated conditions, with a value as high as 9. The photoluminescence spectra of a film of Zeonex doped with **3c** (1% wt.) under air and vacuum are shown in Fig. 2c. This underscores the potential of **3c** as an RTP sensor. Its emission goes from deep blue CIE coordinates (0.17, 0.08) to yellow ones (0.45, 0.49) as the concentration of oxygen decreases (Fig. 2d). Temperature-dependent studies, the results of which are shown in Fig. S13, also corroborate that the yellow emission band derives from RTP instead of thermally activated delayed fluorescence (TADF). The films containing compounds **3b, d** also revealed RTP (Fig. S12), with I_{vac}/I_{air} ratios of 3.8 and 1.7, respectively. Under vacuum, the CIE coordinates of the emission of **3b** are placed within the orange region, while the film containing **3d** exhibits white emission due to its balanced I_{vac}/I_{air} ratio. Therefore, the photoluminescence intensity and color under vacuum can be easily fine-tuned through the molecular design. The introduction of sulfated π -extended

Table 5. Photophysical characterization of compounds **3a–d** in different media.

	$\lambda_{em,sol}$ (nm) ^a	$\Phi_{f,sol}$ (%) ^a	$\lambda_{em,filim}$ (nm) ^b	$\Phi_{f,filim}$ (%) ^b	$\lambda_{em,ZEONEX}$ (nm) ^c	I_{vac}/I_{air} ^d	I_{phos}/I_{FL} ^e	Φ_{air} (%) ^c	Φ_{vac} (%) ^f	Φ_{RTP} (%) ^g	CIE _{air} ^h	CIE _{vac} ^h
DPT ³⁷	394	3.2	449,481	4.7	393 (585)	4.5	4.1	2.7	12.2	9.8	(0.17, 0.04)	(0.47, 0.47)
3a	454,475	14.0	469,491	1.1	456,476 (-)	1.0	-	11	11	-	(0.16, 0.06)	(0.16, 0.06)
3b	402,424	4.2	473	5.9	409,428 (578)	3.8	3.7	4.4	16.7	13.1	(0.16, 0.06)	(0.44, 0.37)
3c	396,414	2.1	449,478	0.8	396,417 (564)	9.0	10.7	1.7	15.3	13.8	(0.17, 0.08)	(0.45, 0.49)
3d	389,408	1.6	462,521	0.3	395 (551)	1.7	1.2	1.5	2.6	1.1	(0.20, 0.14)	(0.34, 0.38)

^a Maximum emission wavelengths ($\lambda_{em,sol}$) at $\lambda_{ex} = 330$ nm and fluorescence quantum yields ($\Phi_{f,sol}$) in toluene, determined using an integrating sphere.

^b Maximum emission wavelengths ($\lambda_{em,filim}$) at $\lambda_{ex} = 330$ nm and fluorescence quantum yields ($\Phi_{f,filim}$) in spin-coated films, determined using an integrating sphere. ^c Maximum emission wavelengths in a Zeonex film ($\lambda_{em,ZEONEX}$) at $\lambda_{ex} = 330$ nm and fluorescence quantum yields under air (Φ_{air}) in Zeonex, measured using an integrating sphere. The values in parenthesis correspond to the maximum wavelength of the RTP band measured under vacuum. ^d

Photoluminescence intensity ratio between vacuum and aerated conditions in Zeonex, calculated as: $I_{vac}/I_{air} = \text{Area}_{vac}/\text{Area}_{air}$. ^e Photoluminescence intensity ratio between the phosphorescence and fluorescence contributions in Zeonex under vacuum, calculated as: $I_{phos}/I_{FL} = \text{Area}_{phos}/\text{Area}_{FL}$. ^f

Photoluminescence quantum yields in Zeonex under vacuum (Φ_{vac}), estimated as $\Phi_{vac} = (I_{vac}/I_{air})\Phi_{air}$. ^g RTP quantum yields in Zeonex under vacuum (Φ_{RTP}), estimated as $\Phi_{RTP} = (I_{phos}/(I_{phos} + I_{FL,vac}))\Phi_{vac}$. ^h CIE 1931 coordinates, calculated from the corresponding photoluminescence spectra under aerated (CIE_{air}) and vacuum (CIE_{vac}) conditions.



ARTICLE

Materials Advances

moieties in **3b** and **3c** afforded the highest RTP quantum yields (Φ_{RTP}) of their molecular mixtures with Zeonex of 13.1 and 13.8%, respectively, surpassing that of the molecular mixture with parent DPT. The photoluminescence spectra of the molecular dispersions of **3b** and **3c** in Zeonex also revealed a clear reduction of the singlet–triplet splitting energy (ΔE_{ST}) with respect to the system containing DPT, as detailed in Figure S14. Specifically, DPT exhibits a ΔE_{ST} of 1.01 eV,³⁸ whereas this value decreases to 0.80 eV for the films with both **3b** and **3c**. A narrower singlet–triplet gap is prone to promoting intersystem crossing, which further supports the enhanced RTP in these two cases. Contrastingly, ΔE_{ST} slightly increases to 1.16 eV for the films with **3d**, which is consistent with its weaker RTP contribution. The films containing precursors **2a–d** do not exhibit RTP, underlining the pivotal role of rigidity conferred through the Scholl reaction. These molecular structures could therefore inspire novel designs towards accessible and efficient halogen- and metal-free RTP emitters.

Conclusions

We synthesized a set of dibenzothiophene-derived heterocycles through a concise and efficient protocol that combines sequential Suzuki–Miyaura and Scholl reactions. The Suzuki–Miyaura couplings were optimized using a mixture of toluene/methanol as solvent, which broadens the substrate scope while affording higher yields. Moreover, it admits a one-pot procedure, further enhancing the efficiency while reducing the number of synthetic steps. This two-step approach, starting from commercially available reagents, permits the construction of complex polycyclic architectures containing up to 11 fused rings with significantly improved overall yields. The resulting π -systems display adjustable photophysical, electrochemical and thermal properties that upgrade those of the parent DPT core. The phenanthrene-containing derivative, with an appropriate IP value of 5.01 eV in the solid state, outperforms as a stable p-type semiconductor in OTFTs exhibiting a μ_{h} of $7 \times 10^{-5} \text{ cm}^2 \text{ V}^{-1} \text{ s}^{-1}$ and an excellent shelf-lifetime exceeding one year under ambient conditions. Moreover, the inclusion of sulfur-rich π -extensions enabled RTP under oxygen-free conditions, achieving quantum yields as high as 14% when dispersed in a Zeonex film. The presence of RTP highly modulates the colour of the photoluminescence from deep blue to yellow-orange as the oxygen content decreases, which entails potential in fields such as lighting and sensing. Overall, this synthetic strategy gives access to multifunctional π -extended materials with potential for optoelectronic applications ranging from p-type semiconductors to molecular sensors.

Author contributions

Clara Fabregat: Methodology, Validation, Formal analysis, Investigation, Data Curation, Writing - Original Draft. Roger Bujaldón: Conceptualization, Methodology, Validation, Investigation, Writing - Original Draft, Writing - Review & Editing, Visualization. Sílvia Oliva: Validation, Investigation. Jaume Garcia-Amorós: Validation, Writing -

Review & Editing, Supervision, Project administration. Dmytro Volyniuk: Methodology, Formal analysis, Investigation, Data Curation. Melika Ghasemi: Investigation, Data Curation. Juozas V. Grazulevicius: Resources, Writing - Review & Editing, Supervision, Funding acquisition. Joaquim Puigdollers: Resources, Writing - Review & Editing, Supervision. Dolores Velasco: Conceptualization, Resources, Writing - Review & Editing, Supervision, Project administration, Funding acquisition.

Conflicts of interest

There are no conflicts to declare.

Data availability

The data supporting this article have been included as part of the Supplementary Information.

Acknowledgements

Authors gratefully acknowledge financial support by Ministerio de Ciencia, Innovación y Universidades (grant number PID2023-151915NB-I00) and Horizon Europe, the European Union's framework programme for research and innovation (R&I) for 2021-2027, project HELIOS (grant agreement No 101155017). C.F is grateful for the predoctoral grant FI AGAUR from Generalitat de Catalunya. The authors also want to thank the CCITUB for the use of their equipment, and especially acknowledge Cristina Puigjaner (X-Ray Diffraction Unit) for the elucidation of the single-crystal structures and M^a Antònia Molins and Vicky Muñoz (NMR unit) for their assistance with 2D NMR spectroscopy.

References

- 1 M. Sawatzki-Park, S.-J. Wang, H. Kleemann and K. Leo, *Chem. Rev.*, 2023, **123**, 8232–8250.
- 2 F. Wu, Y. Liu, J. Zhang, S. Duan, D. Ji and H. Yang, *Small Methods*, 2021, **5**, 2100676.
- 3 A. D. Scaccabarozzi, A. Basu, F. Aniés, J. Liu, O. Zapata-Arteaga, R. Warren, Y. Firdaus, M. I. Nugraha, Y. Lin, M. Campoy-Quiles, N. Koch, C. Müller, L. Tsetseris, M. Heeney and T. D. Anthopoulos, *Chem. Rev.*, 2021, **122**, 4420–4492.
- 4 H. Bronstein, C. B. Nielsen, B. C. Schroeder and I. McCulloch, *Nat. Rev. Chem.*, 2020, **4**, 66.
- 5 S. M. Elbert, E. Bolgert, O. T. A. Paine, F. Ghalami, W.-S. Zhang, U. Zschieschang, F. Rominger, D. Popp, H. Klauk, M. Elstner and M. Mastalerz, *Org. Chem. Front.*, 2024, **11**, 5340.
- 6 H. Shudo, P. Wiesener, E. Kolodzeiski, K. Mizukami, D. Imoto, H. Mönig, S. Amirjalayer, H. Sakamoto, H. Klaasen, B. J. Ravoo, N. Kimizuka, A. Yagi and K. Itami, *Nat. Commun.*, 2025, **16**, 1074.
- 7 H. M. F. Elnagdy, *Dyes Pigm.*, 2024, **229**, 112251.
- 8 A. Cuadrado, R. Bujaldón, C. Fabregat, J. Puigdollers and D. Velasco, *Org. Electron.*, 2024, **107**, 107020.
- 9 A. Nitti, M. Scagliotti, L. Beverina, L. Mariucci, M. Rapisarda and D. Pasini, *Mater. Adv.*, 2023, **4**, 4590–4597.
- 10 A. Babuji, I. Temiño, A. Pérez-Rodríguez, O. Solomeshch, N. Tessler, M. Vila, J. Li, M. Mas-Torrent, C. Ocal and E. Barrena, *ACS Appl. Mater. Interfaces*, 2020, **12**, 28416.



- 11 B. Lu, S. Zhang, D. Liu, W. Jin, D. Li, Z. Liu and T. He, *Org. Chem. Front.*, 2025, **12**, 422.
- 12 Y. Yuan, G. Giri, A. L. Ayzner, A. P. Zoombelt, S. C. B. Mannsfeld, J. Chen, D. Nordlund, M. F. Toney, J. Huang and Z. Bao, *Nat. Commun.*, 2014, **5**, 3005.
- 13 H. Iino, T. Usui and J. Hanna, *Nat. Commun.*, 2015, **6**, 6828.
- 14 A. Y. Amin, A. Khassanov, K. Reuter, T. Meyer-Friedrichsen and M. Halik, *J. Am. Chem. Soc.*, 2012, **134**, 16548.
- 15 T. Yamamoto and K. Takimiya, *J. Am. Chem. Soc.*, 2007, **129**, 2224.
- 16 J. W. Borchert, B. Peng, F. Letzkus, J. N. Burghartz, P. K. L. Chan, K. Zojer, S. Ludwigs and H. Klauk, *Nat. Commun.*, 2019, **10**, 1119.
- 17 B. Peng, K. Cao, A. H. Y. Lau, M. Chen, Y. Lu and P. K. L. Chan, *Adv. Mater.*, 2020, **32**, 2002281.
- 18 K. Nakayama, Y. Hirose, J. Soeda, M. Yoshizumi, T. Uemura, M. Uno, W. Li, M. J. Kang, M. Yamagishi, Y. Okada, E. Miyazaki, Y. Nakazawa, A. Nakao, K. Takimiya and J. Takeya, *Adv. Mater.*, 2011, **23**, 1626.
- 19 G. M. Badger, B. J. Christie, J. M. Pryke and W. H. F. Sasse, *J. Chem. Soc.*, 1957, 4417–4419.
- 20 S. Venkateswarlu, S. P. Prakoso, S. Kumar and Y.-T. Tao, *J. Chin. Chem. Soc.*, 2020, **67**, 437–445.
- 21 S. Venkateswarlu, S. Kumar and Y.-T. Tao, *Asian J. Org. Chem.*, 2021, **10**, 2251–2261.
- 22 S. Venkateswarlu, S. P. Prakoso, S. Kumar, M.-Y. Kuo and Y.-T. Tao, *J. Org. Chem.*, 2019, **84**, 10990.
- 23 S. Maddala, K. Kollimalaiaian, A. Samal and V. Parthasarathy, *Tetrahedron*, 2024, **151**, 133807.
- 24 M. Sankarrao, S. Maddala and V. Parthasarathy, *Adv. Synth. Catal.*, 2024, **366**, 4114–4121.
- 25 S. Maddala, S. Mahanthi and V. Parthasarathy, *Chem. Eur. J.*, 2025, **31**, e01724.
- 26 C.-X. Liu, H. Wang, J.-Q. Du, K.-Q. Zhao, P. Hu, B.-Q. Wang, H. Monobe, B. Heinrich and B. Donnio, *J. Mater. Chem. C*, 2018, **6**, 4471–4478.
- 27 J.-F. Hang, H. Lin, K.-Q. Zhao, P. Hu, B.-Q. Wang, H. Monobe, C. Zhu and B. Donnio, *Eur. J. Org. Chem.*, 2021, 1989–2002.
- 28 T. Ma, H.-F. Wang, K.-Q. Zhao, B.-Q. Wang, P. Hu, H. Monobe, B. Heinrich and B. Donnio, *ChemPlusChem*, 2019, **84**, 1439–1448.
- 29 C.-Y. Zeng, W.-J. Deng, K.-Q. Zhao, C. Redshaw and B. Donnio, *Chem. Eur. J.*, 2024, **30**, e202400296.
- 30 T. Ma, Y.-J. Zhong, H.-F. Wang, K.-Q. Zhao, B.-Q. Wang, P. Hu, H. Monobe and B. Donnio, *Chem. Asian J.*, 2021, **16**, 1106–1117.
- 31 W.-J. Deng, S. Liu, H. Lin, K.-X. Zhao, X.-Y. Bai, K.-Q. Zhao, P. Hu, B.-Q. Wang, H. Monobe and B. Donnio, *New J. Chem.*, 2022, **46**, 7936–7949.
- 32 K.-C. Zhao, J.-Q. Du, H.-F. Wang, K.-Q. Zhao, P. Hu, B.-Q. Wang, H. Monobe, B. Heinrich and B. Donnio, *Chem. Asian J.*, 2019, **14**, 462–470.
- 33 S. Venkateswarlu, Y.-D. Lin, K.-M. Lee, K.-L. Liao and Y.-T. Tao, *ACS Appl. Mater. Interfaces*, 2020, **12**, 50495.
- 34 M. Nagase, R. Yoshida, S. Nakano, T. Hirose and Y. Segawa, *Chem. Commun.*, 2025, **61**, 11187–11190.
- 35 L. Ueberricke and M. Mastalerz, *Chem. Rec.*, 2021, **21**, 558.
- 36 L. Fang, Y. Zhang, Y. Cai, J. Zhang, Y. Wei, Y. Yuan and P. Wang, *Energy Environ. Sci.*, 2023, **16**, 5231.
- 37 L. Knight, J. C. Jimenez, Q. Tran, M. Zhao, M. H. Pugh, C. D. Brancel, H. Zhang, R. Li, Y. Yuan, Y. Li, L. Zhu and G. Sauvé, *Mater. Adv.*, 2024, **5**, 6145–6153.
- 38 C. Fabregat, R. Bujaldón, J. Garcia-Amorós, D. Volyniuk, M. Ghasemi, J. V. Grazulevicius and D. Velasco, *Dyes Pigm.*, 2025, **243**, 113053.
- 39 Z. Xu, D. Hean, J. Yuan and M. O. Wolf, Recent Progress in Pure Organic Room Temperature Phosphorescence of Small Molecular Host–Guest Systems, *ACS Mater. Lett.*, 2021, **3**, 652–657. DOI: 10.1039/D5MA01124H
- 40 P. Pander, A. Swist, J. Soloducho and F. B. Dias, *Dyes Pigm.*, 2017, **142**, 315–322.
- 41 S. Han, Y. Li, Z. Wang and X. Li, *Dyes Pigm.*, 2024, **228**, 112243.
- 42 Y. Wang, X. Qi, Z. Ye, Y. Yan, Q. Chen and Y. Yang, *Dyes Pigm.*, 2024, **224**, 112486.
- 43 H. Bhatia and D. Ray, *Mater. Adv.*, 2020, **1**, 1858–1865.
- 44 J. Wang, H. Xu, B. Li, X.-P. Cao and H.-L. Zhang, *Tetrahedron*, 2012, **68**, 1192.
- 45 W. Cai, J. Lee, Y. Zhao, B. Kang and G. Zhang, *Mater. Adv.*, 2023, **4**, 3344–3350.
- 46 R. Bujaldón, A. Vilche, J. Puigdollers, C. Puigjaner, X. Alcobé and D. Velasco, *ACS Appl. Electron. Mater.*, 2023, **5**, 3675–3684.
- 47 R. Bujaldón, A. Cuadrado, D. Volyniuk, J. V. Grazulevicius, J. Puigdollers and D. Velasco, *Coatings*, 2023, **13**, 896.
- 48 M. Reig, G. Bagdziunas, A. Ramanavicius, J. Puigdollers and D. Velasco, *Phys. Chem. Chem. Phys.*, 2018, **20**, 17889–17898.
- 49 T. Lei, J.-Y. Wang and J. Pei, *Chem. Mater.*, 2014, **26**, 594–603.
- 50 J. C. Jimenez, Q. Tran, M. H. Pugh, C. D. Brancel, A. L. Rheingold and G. Sauvé, *Dyes Pigm.*, 2023, **208**, 110858.
- 51 K. M. Saini, R. K. Saunthwal, A. K. Verma, *Org. Biomol. Chem.*, 2017, **15**, 10289–10298.
- 52 T. T. Dang, T. T. Dang, N. Rasool, A. Villinger, H. Reinke, C. Fischer and P. Langer, *Adv. Synth. Catal.*, 2009, **351**, 1595–1609.
- 53 X. Liu, Y. Wang, J. Gao, L. Jiang, X. Qi, W. Hao, S. Zou, H. Zhang, H. Li and W. Hu, *Chem. Commun.*, 2014, **50**, 442.
- 54 J. Urieta-Mora, I. Zimmermann, J. Aragó, A. Molina-Ontoria, E. Ortí, N. Martín and M. K. Nazeeruddin, *Chem. Mater.*, 2019, **31**, 6435.
- 55 Y. Xing, X. Xu, F. Wang and P. Lu, *Opt. Mater.*, 2006, **29**, 407.
- 56 H. Muraoka, T. Tanifuji and S. Ogawa, *Chem. Lett.*, 2011, **40**, 964.
- 57 C. M. Cardona, W. Li, A. E. Kaifer, D. Stockdale and G. C. Bazan, *Adv. Mater.*, 2011, **23**, 2367–2371.
- 58 S. Kumar and Y.-T. Tao, *J. Org. Chem.*, 2015, **80**, 5066.
- 59 J. Sherwood, J. H. Clark, I. J. S. Fairlamb and J. M. Slatery, *Green Chem.*, 2019, **21**, 2164.
- 60 Z. Ahmadi and J. S. McIndoe, *Chem. Commun.*, 2013, **49**, 11488.
- 61 S. T. Handy, H. Bregman, J. Lewis, X. Zhang and Y. Zhang, *Tetrahedron Lett.*, 2003, **44**, 427.
- 62 L. Jedinák, R. Zátoková, H. Zemánková, A. Šustková and P. Cankář, *J. Org. Chem.*, 2017, **82**, 157.
- 63 S. T. Handy and D. Mayi, *Tetrahedron Lett.*, 2007, **48**, 8108.
- 64 S. Maddala, A. Panua and P. Venkatakrishnan, *Chem. Eur. J.*, 2021, **27**, 16013–16020.
- 65 C.-H. Lee and K. N. Plunkett, *Org. Lett.*, 2013, **15**, 1202–1205.
- 66 J. E. Campbell, J. Yang and G. M. Day, *J. Mater. Chem. C*, 2017, **5**, 7574.
- 67 G. R. Desiraju and A. Gavezzotti, *Acta Cryst.*, 1989, **B45**, 473.
- 68 S. Fritz, T. M. Kraft, M. Sommer and J. C. Brendel, *Appl. Phys. A*, 2015, **118**, 809–815.
- 69 M. M. Hasan, M. M. Islam, X. Li, M. He, R. Manley, J. Chang, N. Zhelev, K. Mehrotra and J. Jang, *IEEE Trans. Electron Devices*, 2020, **67**, 1751–1756.

View Article Online
DOI: 10.1039/D5MA01124H

DATA AVAILABILITY STATEMENT

- The data supporting this article have been included as part of the Supplementary Information.

